

MAGNETIC FIELDS TOWARDS OPHIUCHUS-B DERIVED FROM SCUBA-2 POLARIZATION
MEASUREMENTS

ARCHANA SOAM,¹ KATE PATTLE,^{2,3,4} DEREK WARD-THOMPSON,² CHANG WON LEE,^{1,5} SARAH SADAVOY,⁶
PATRICK M. KOCH,⁷ GWANJEONG KIM,^{1,5,8} JUNGMI KWON,⁹ WOJIN KWON,^{1,5} DORIS ARZOUMANIAN,¹⁰ DAVID BERRY,¹¹
THIEM HOANG,^{1,5} MOTOHIDE TAMURA,^{12,13,3} SANG-SUNG LEE,^{1,5} TIE LIU,^{1,11} KEE-TAE KIM,¹ DOUG JOHNSTONE,^{14,15}
FUMITAKA NAKAMURA,^{16,17} A-RAN LYO,¹ TAKASHI ONAKA,¹² JONGSOO KIM,^{1,5} RAY S. FURUYA,^{18,19} TETSUO HASEGAWA,³
SHIH-PING LAI,^{4,7} PIERRE BASTIEN,²⁰ EUN JUNG CHUNG,¹ SHINYOUNG KIM,^{1,5} HARRIET PARSONS,¹¹ MARK G. RAWLINGS,¹¹
STEVE MAIRS,¹¹ SARAH F. GRAVES,¹¹ JEAN-FRANCOIS ROBITAILLE,²¹ HONG-LI LIU,²² ANTHONY P. WHITWORTH,²³
CHAKALI ESWARAIHAH,⁴ RAMPRASAD RAO,⁷ HYUNJU YOO,²⁴ MARTIN HOUE,²⁵ JI-HYUN KANG,²⁶ YASUO DOI,²⁷
MINHO CHOI,¹ MIJU KANG,¹ SIMON COUDÉ,²⁰ HUA-BAI LI,²² MASAFUMI MATSUMURA,²⁸ BRENDA C. MATTHEWS,^{14,15}
ANDY PON,²⁵ JAMES DI FRANCESCO,^{14,15} SAEKO S. HAYASHI,²⁹ KOJI S. KAWABATA,^{30,31,32} SHU-ICHIRO INUTSUKA,¹⁰
KEPING QIU,^{33,34} ERICA FRANZMANN,³⁵ PER FRIBERG,¹¹ JANE S. GREAVES,²³ JASON M. KIRK,² DI LI,³⁶
HIROKO SHINNAGA,³⁷ SVEN VAN LOO,³⁸ YUSUKE ASO,¹² DO-YOUNG BYUN,^{26,5} HUEI-RU CHEN,^{4,7} MIKE C.-Y. CHEN,¹⁵
WEN PING CHEN,³⁹ TAO-CHUNG CHING,^{36,40} JUNGYEON CHO,²⁴ ANTONIO CHRYSOSTOMOU,⁴¹ EMILY DRABEK-MAUNDER,²³
STEWART P. S. EYRES,² JASON FIEGE,³⁵ RACHEL K. FRIESEN,⁴² GARY FULLER,²¹ TIM GLEDHILL,⁴¹ MATT J. GRIFFIN,²³
QILAO GU,²² JENNIFER HATCHELL,⁴³ WAYNE HOLLAND,^{44,45} TSUYOSHI INOUE,¹⁰ KAZUNARI IWASAKI,⁴⁶ IL-GYO JEONG,¹
SUNG-JU KANG,¹ FRANCISCA KEMPER,⁷ KYOUNG HEE KIM,⁴⁷ MI-RYANG KIM,¹ KEVIN M. LACAILLE,^{48,49}
JEONG-EUN LEE,⁵⁰ DALEI LI,⁵¹ JUNHAO LIU,^{33,34} SHENG-YUAN LIU,⁷ GERALD H. MORIARTY-SCHIEVEN,¹⁴
HIROYUKI NAKANISHI,³⁷ NAGAYOSHI OHASHI,²⁹ NICOLAS PERETTO,²³ TAE-SOO PYO,^{29,17} LEI QIAN,⁴⁰ BRENDAN RETTER,²³
JOHN RICHER,^{52,53} ANDREW RIGBY,²³ GIORGIO SAVINI,⁵⁴ ANNA M. M. SCAIFE,²¹ YA-WEN TANG,⁷ KOHJI TOMISAKA,^{16,17}
HONGCHI WANG,⁵⁵ JIA-WEI WANG,⁴ HSI-WEI YEN,^{7,56} JINGHUA YUAN,⁴⁰ CHUAN-PENG ZHANG,⁴⁰ GUOYIN ZHANG,⁴⁰
JIANJUN ZHOU,⁵¹ LEI ZHU,⁴⁰ PHILIPPE ANDRÉ,⁵⁷ C. DARREN DOWELL,⁵⁸ SAM FALLE,⁵⁹ YUSUKE TSUKAMOTO,³⁷
YOSHIHIRO KANAMORI,²⁷ AKIMASA KATAOKA,¹⁶ MASATO I.N. KOBAYASHI,¹⁰ TETSUYA NAGATA,⁶⁰ HIRO SAITO,⁶¹
MASUMICHI SETA,⁶² JIHYE HWANG,^{1,5} ILSEUNG HAN,^{1,5} HYESEUNG LEE,²⁴ AND TETSUYA ZENKO⁶⁰

¹Korea Astronomy and Space Science Institute, 776 Daedeokdae-ro, Yuseong-gu, Daejeon 34055, Republic of Korea

²Jeremiah Horrocks Institute, University of Central Lancashire, Preston PR1 2HE, UK

³National Astronomical Observatory of Japan, National Institutes of Natural Sciences, Osawa, Mitaka, Tokyo 181-8588, Japan

⁴Institute of Astronomy and Department of Physics, National Tsing Hua University, Hsinchu 30013, Taiwan

⁵Korea University of Science and Technology, 217 Gajang-ro, Yuseong-gu, Daejeon 34113, Korea

⁶Harvard-Smithsonian Center for Astrophysics, 60 Garden Street, Cambridge, MA 02138, USA

⁷Academia Sinica Institute of Astronomy and Astrophysics, P.O. Box 23-141, Taipei 10617, Taiwan

⁸Nobeyama Radio Observatory (NRO), National Astronomical Observatory of Japan (NAOJ), Japan

⁹Institute of Space and Astronautical Science, Japan Aerospace Exploration Agency, 3-1-1 Yoshinodai, Chuo-ku, Sagami-hara, Kanagawa 252-5210, Japan

¹⁰Department of Physics, Graduate School of Science, Nagoya University, Furo-cho, Chikusa-ku, Nagoya 464-8602, Japan

¹¹East Asian Observatory, 660 N. A'ohōkū Place, University Park, Hilo, HI 96720, USA

¹²Department of Astronomy, Graduate School of Science, The University of Tokyo, 7-3-1 Hongo, Bunkyo-ku, Tokyo 113-0033, Japan

¹³Astrobiology Center, National Institutes of Natural Sciences, 2-21-1 Osawa, Mitaka, Tokyo 181-8588, Japan

¹⁴NRC Herzberg Astronomy and Astrophysics, 5071 West Saanich Road, Victoria, BC V9E 2E7, Canada

¹⁵Department of Physics and Astronomy, University of Victoria, Victoria, BC V8P 1A1, Canada

¹⁶Division of Theoretical Astronomy, National Astronomical Observatory of Japan, Mitaka, Tokyo 181-8588, Japan

¹⁷SOKENDAI (The Graduate University for Advanced Studies), Hayama, Kanagawa 240-0193, Japan

¹⁸Tokushima University, Minami Jousanajima-machi 1-1, Tokushima 770-8502, Japan

¹⁹Institute of Liberal Arts and Sciences Tokushima University, Minami Jousanajima-machi 1-1, Tokushima 770-8502, Japan

- ²⁰Centre de recherche en astrophysique du Québec & département de physique, Université de Montréal, C.P. 6128, Succ. Centre-ville, Montréal, QC, H3C 3J7, Canada
- ²¹Jodrell Bank Centre for Astrophysics, School of Physics and Astronomy, University of Manchester, Oxford Road, Manchester, M13 9PL, UK
- ²²Department of Physics, The Chinese University of Hong Kong, Shatin, N.T., Hong Kong
- ²³School of Physics and Astronomy, Cardiff University, The Parade, Cardiff, CF24 3AA, UK
- ²⁴Department of Astronomy and Space Science, Chungnam National University, 99 Daehak-ro, Yuseong-gu, Daejeon 34134, Korea
- ²⁵Department of Physics and Astronomy, The University of Western Ontario, 1151 Richmond Street, London N6A 3K7, Canada
- ²⁶Korea Astronomy and Space Science Institute, 776 Daedeokdae-ro, Yuseong-gu, Daejeon 34055, Korea
- ²⁷Department of Earth Science and Astronomy, Graduate School of Arts and Sciences, The University of Tokyo, 3-8-1 Komaba, Meguro, Tokyo 153-8902, Japan
- ²⁸Kagawa University, Saiwai-cho 1-1, Takamatsu, Kagawa, 760-8522, Japan
- ²⁹Subaru Telescope, National Astronomical Observatory of Japan, 650 N. A'ohōkū Place, Hilo, HI 96720, USA
- ³⁰Hiroshima Astrophysical Science Center, Hiroshima University, Kagamiyama 1-3-1, Higashi-Hiroshima, Hiroshima 739-8526, Japan
- ³¹Department of Physics, Hiroshima University, Kagamiyama 1-3-1, Higashi-Hiroshima, Hiroshima 739-8526, Japan
- ³²Core Research for Energetic Universe (CORE-U), Hiroshima University, Kagamiyama 1-3-1, Higashi-Hiroshima, Hiroshima 739-8526, Japan
- ³³School of Astronomy and Space Science, Nanjing University, 163 Xianlin Avenue, Nanjing 210023, China
- ³⁴Key Laboratory of Modern Astronomy and Astrophysics (Nanjing University), Ministry of Education, Nanjing 210023, China
- ³⁵Department of Physics and Astronomy, The University of Manitoba, Winnipeg, Manitoba R3T2N2, Canada
- ³⁶CAS Key Laboratory of FAST, National Astronomical Observatories, Chinese Academy of Sciences
- ³⁷Department of Physics and Astronomy, Graduate School of Science and Engineering, Kagoshima University, 1-21-35 Korimoto, Kagoshima 890-0065, JAPAN
- ³⁸School of Physics and Astronomy, University of Leeds, Woodhouse Lane, Leeds LS2 9JT, UK
- ³⁹Institute of Astronomy, National Central University, Chung-Li 32054, Taiwan
- ⁴⁰National Astronomical Observatories, Chinese Academy of Sciences, A20 Datun Road, Chaoyang District, Beijing 100012, China
- ⁴¹School of Physics, Astronomy & Mathematics, University of Hertfordshire, College Lane, Hatfield, Hertfordshire AL10 9AB, UK
- ⁴²National Radio Astronomy Observatory, 520 Edgemont Rd., Charlottesville VA USA 22903
- ⁴³Physics and Astronomy, University of Exeter, Stocker Road, Exeter EX4 4QL, UK
- ⁴⁴UK Astronomy Technology Centre, Royal Observatory, Blackford Hill, Edinburgh EH9 3HJ, UK
- ⁴⁵Institute for Astronomy, University of Edinburgh, Royal Observatory, Blackford Hill, Edinburgh EH9 3HJ, UK
- ⁴⁶Department of Environmental Systems Science, Doshisha University, Tatara, Miyakodani 1-3, Kyotanabe, Kyoto 610-0394, Japan
- ⁴⁷Department of Earth Science Education, Kongju National University, 56 Gongjudaehak-ro, Gongju-si, Chungcheongnam-do 32588, Korea
- ⁴⁸Department of Physics and Astronomy, McMaster University, Hamilton, ON L8S 4M1 Canada
- ⁴⁹Department of Physics and Atmospheric Science, Dalhousie University, Halifax B3H 4R2, Canada
- ⁵⁰School of Space Research, Kyung Hee University, 1732 Deogyong-daero, Giheung-gu, Yongin-si, Gyeonggi-do 17104, Korea
- ⁵¹Xinjiang Astronomical Observatory, Chinese Academy of Sciences, 150 Science 1-Street, Urumqi 830011, Xinjiang, China
- ⁵²Astrophysics Group, Cavendish Laboratory, J J Thomson Avenue, Cambridge CB3 0HE, UK
- ⁵³Kavli Institute for Cosmology, Institute of Astronomy, University of Cambridge, Madingley Road, Cambridge, CB3 0HA, UK
- ⁵⁴OSL, Physics & Astronomy Dept., University College London, WC1E 6BT London, UK
- ⁵⁵Purple Mountain Observatory, Chinese Academy of Sciences, 2 West Beijing Road, 210008 Nanjing, PR China
- ⁵⁶European Southern Observatory (ESO), Karl-Schwarzschild-Strae 2, D-85748 Garching, Germany
- ⁵⁷Laboratoire AIM CEA/DSM-CNRS-Universit Paris Diderot, IRFU/Service d'Astrophysique, CEA Saclay, F-91191 Gif-sur-Yvette, France
- ⁵⁸Jet Propulsion Laboratory, M/S 169-506, 4800 Oak Grove Drive, Pasadena, CA 91109, USA
- ⁵⁹Department of Applied Mathematics, University of Leeds, Woodhouse Lane, Leeds LS2 9JT, UK
- ⁶⁰Department of Astronomy, Graduate School of Science, Kyoto University, Sakyo-ku, Kyoto 606-8502, Japan
- ⁶¹Department of Astronomy and Earth Sciences, Tokyo Gakugei University, Koganei, Tokyo 184-8501, Japan
- ⁶²Department of Physics, School of Science and Technology, Kwansei Gakuin University, 2-1 Gakuen, Sanda, Hyogo 669-1337, Japan

(Received —; Revised —; Accepted —)

ABSTRACT

We present the results of dust emission polarization measurements of Ophiuchus-B (Oph-B) carried out using the Submillimetre Common-User Bolometer Array 2 (SCUBA-2) camera with its associated polarimeter (POL-2) on

the James Clerk Maxwell Telescope (JCMT) in Hawaii. This work is part of the B-fields In Star-forming Region Observations (BISTRO) survey initiated to understand the role of magnetic fields in star formation for nearby star-forming molecular clouds. We present a first look at the geometry and strength of magnetic fields in Oph-B. The field geometry is traced over ~ 0.2 pc, with clear detection of both of the sub-clumps of Oph-B. The field pattern appears significantly disordered in sub-clump Oph-B1. The field geometry in Oph-B2 is more ordered, with a tendency to be along the major axis of the clump, parallel to the filamentary structure within which it lies. The degree of polarization decreases systematically towards the dense core material in the two sub-clumps. The field lines in the lower density material along the periphery are smoothly joined to the large scale magnetic fields probed by NIR polarization observations. We estimated a magnetic field strength of $630 \pm 410 \mu\text{G}$ in the Oph-B2 sub-clump using a Davis-Chandrasekhar-Fermi analysis. With this magnetic field strength, we find a mass-to-flux ratio $\lambda = 1.6 \pm 1.1$, which suggests that the Oph-B2 clump is slightly magnetically supercritical.

Keywords: polarization, dust emission

1. INTRODUCTION

Low mass stars are formed in dense cores ($M \approx 1 - 10 M_{\odot}$, size $\approx 0.1-0.4$ pc and density $\approx 10^4 - 10^5 \text{cm}^{-3}$) embedded in molecular clouds which are generally self-gravitating, turbulent, magnetized and thought to be compressible fluids and are expected to form one or a few stars when they become unstable to gravitational collapse.

Considering the magnetized nature of molecular clouds (Shu et al., 1987; McKee & Ostriker, 2007), we expect magnetic fields (B-fields) to also have a significant impact on dense cores. Nevertheless, the role of B-fields on the formation of dense cores and their evolution into the various stages of star formation is still under debate. Several observational and theoretical studies have been dedicated to understand the importance of B-fields in star formation. For example, isolated low-mass cores that are magnetically dominated may gradually condense out of a large scale cloud through ambipolar diffusion (e.g., Shu et al., 1987; McKee et al., 1993; Mouschovias & Ciolek, 1999; Allen et al., 2003). In this picture, the core will be flattened into a disk-like morphology on scales of a few thousand AU, with field lines primarily parallel to the symmetry axis. These field lines become pinched into an hour-glass morphology as mass accumulates in the core and self-gravity becomes more significant (Fiedler & Mouschovias, 1993; Galli & Shu, 1993; Girart et al., 2006; Attard et al., 2009). On the other hand, B-fields are expected to be less significant if cores form via turbulent flows (Mac Low & Klessen, 2004; Dib et al., 2007, 2010). In this picture the B-field morphology will be more chaotic (Crutcher, 2004; Hull et al., 2017a).

B-fields are often characterized by dust polarization observations. Dust grains are expected to align with their short axes parallel to an external B-field. As a result, thermal dust emission at sub-millimeter or millimeter wavelengths from these grains will be polarized perpendicular to the B-field (e.g. Cudlip et al., 1982; Hildebrand et al., 1984; Hildebrand, 1988; Rao et al., 1998; Lazarian, 2000; Dotson et al., 2000, 2010; Vaillancourt & Matthews, 2012; Hull et al., 2014). The actual mechanism by which dust grains align with a B-field is still unclear (Lazarian, 2007; Andersson et al., 2015). The most accepted mechanism to date is radiative torque alignment (e.g. Hoang & Lazarian, 2014; Hoang et al., 2015; Andersson et al., 2015), which was originally proposed by Dolginov & Mitrofanov (1976).

Polarized thermal dust emission is important because it probes the magnetic fields in the denser regions with extinction $A_V > 50$ mag, since NIR/optical polariza-

tion measurements are limited by the number of detectable background stars and cannot probe these high density environments. At sub-mm wavelength one can probe the B-field morphology deep inside the dense cores ($n_{\text{H}_2} \sim 10^5 - 10^6 \text{cm}^{-3}$) where the central protostars and their circumstellar disks form. B-fields in more diffuse medium ($A_V \sim 1-20$ mag), associated with larger-scale structures (>1 pc), can typically be probed using dust extinction polarization of background stars at optical or NIR wavelengths (Hall, 1949; Hiltner, 1949a,b).

Ophiuchus is a molecular cloud at a distance of ≈ 140 pc (e.g. Chini, 1981; de Geus et al., 1989; Knude & Hog, 1998; Rebull et al., 2004; Loinard et al., 2008; Ortiz-León et al., 2017). Therefore this is one of the closest low mass star forming regions (Wilking, 1992; Johnstone et al., 2000; Padgett et al., 2008; Miville-Deschênes et al., 2010). The Ophiuchus region is highly structured, with several ~ 1 pc sized clumps. This study focuses on the Oph-B clump, which has two active star forming sub-regions named Oph-B1 and Oph-B2, separated by $\sim 5'$. The Oph-B2 clump is the second densest region in Ophiuchus.

We present the first submm polarization observations made using the Submillimetre Common-User Bolometer Array 2 (SCUBA-2) camera with the POL-2 polarimeter towards the Oph-B region to map the B-fields on core scales. The molecular line observations towards this region using the Heterodyne Array Receiver Program (HARP) are already available in White et al. (2015) to understand the kinematics of the cloud.

The paper is organized as follows: in Section 2, we describe the observations and data reduction; in Section 3, we give initial results; in Section 4, we analyze the polarization data and estimate the magnetic field strength; and in Section 5 we summarize the paper.

2. DATA ACQUISITION AND REDUCTION TECHNIQUES

We observed Oph-B in 850- μm polarized emission with SCUBA-2 (Holland et al., 2013) in conjunction with POL-2 (Friberg et al., 2016; P.Bastien et al. in prep., 2018) as part of the B-fields In STar-forming Region Observations (Ward-Thompson et al., 2017) survey under project code M16AL004 at the James Clerk Maxwell Telescope (JCMT). This survey aims to use dust polarization maps of nearby molecular clouds to probe B-field structures. Oph-B was observed over a series of 21 observations, with an average integration time of ~ 0.55 hours per observation, in good weather ($0.05 < \tau_{225} < 0.08$, where τ_{225} is atmospheric opacity at 225 GHz). Table 1 summarizes the observation logs. The scan pattern used was a POL-2 daisy (Friberg et al., 2016)

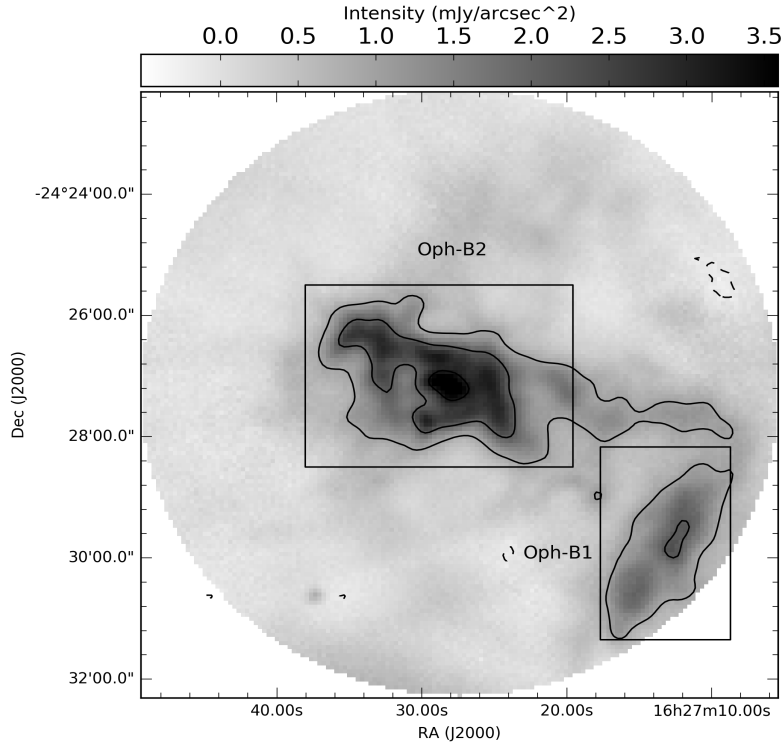


Figure 1. The 850 μ m dust emission map of Oph-B clump obtained using SCUBA-2 on the JCMT. The two sub-clumps, B1 and B2, are labeled with boxes. Contours are of 850 μ m emission (greyscale) and the contour levels are drawn with (0.6, 1.8, 2.9, 4.1) mJy/arcsec².

Table 1. Log of SCUBA-2/POL-2 observations.

No. of Observations	Observation date (year, month, date)
3	2016 Apr. 27
3	2016 Apr. 28
5	2016 May 02
1	2016 May 05
5	2016 May 07
2	2016 May 10
2	2016 May 11

producing a uniform, high signal-to-noise, coverage over the central 3' of the map.. This observing mode is based on the SCUBA-2 CV daisy scan pattern (Holland et al., 2013) but modified to have a slower scan speed (8''/s compared to 155''/s) to obtain sufficient on-sky data for good Stokes Q and U values. This pattern maps a fully sampled, 12'-diameter, circular region with an effective resolution of 14.1''. Coverage decreases, with a consequent significant increase in the RMS noise, towards the edges of the map. The wave plate rotates at a frequency of 2 Hz.

The data were reduced using the `pol2map` python script in the Starlink (Currie et al., 2014) SMURF (Jenness et al., 2013) package. The reduction followed three main steps. In step one, `pol2map` uses the `calcqu` command to create Stokes Q , U and I timestreams from the raw data. It then creates an initial Stokes I map for each of the observations using the `makemap` (Chapin et al., 2013) routine, and coadds these to create an initial estimate of the Stokes I emission in the region. In step two, `pol2map` is re-run. The initial I map of the region is used to generate a fixed signal-to-noise-based mask which is used to define regions of astrophysical emission and thus to consistently re-reduce the previously-created Stokes I timestreams for each observation (see Chapin et al. 2013 for a detailed discussion on `makemap` and Mairs et al. (2015) for the role of masking in SCUBA-2 data reduction). The new set of Stokes I maps are then coadded to produce the final Stokes I emission map of the region. In step 3, `pol2map` is again re-run, this time creating a Stokes Q and U maps for each observation from their timestreams, using the same mask as used in step 2, and coadding these to produce final Stokes Q and U emission maps for the region. The final Stokes Q , U and I maps, and their corresponding variance maps, are then used to create a polarization vector catalog. The vectors are de-biased to remove the

effect of statistical biasing in low signal-to-noise-ratio (SNR) regions. See [Mairs et al. \(2015\)](#) and [Pattle et al. \(2017\)](#) for a detailed description of the SCUBA-2 and POL-2 data reduction process, respectively.

The RMS noise in the maps was estimated by selecting an emission-free region near the map center and finding the standard deviation of the measured flux density distribution in that region. A RMS noise value of ~ 2 mJy/beam ([Pattle et al., 2017](#)) was set as the target value for the BISTRO survey. The estimated noise in the Stokes I map of Oph-B is ~ 3.5 mJy/beam.

Bias in the measured polarization fraction and polarized intensity values result from the fact that polarized intensity is defined as being positive, and so uncertainties on Stokes Q and U values tend to increase the measured polarization values ([Vaillancourt, 2006](#); [Kwon et al., 2018](#)). De-biased values of polarized intensity are estimated to be

$$PI = \sqrt{Q^2 + U^2 - 0.5(\delta Q^2 + \delta U^2)}, \quad (1)$$

where PI is polarized intensity, δQ is the uncertainty on Stokes Q, and δU is the uncertainty on Stokes U. The polarization fraction, P, is then given by

$$P = \frac{PI}{I}, \quad (2)$$

where I is the total intensity.

The polarization position angle θ and the corresponding uncertainties ([Naghizadeh-Khouei & Clarke, 1993](#)) are estimated as:

$$\theta = \frac{1}{2} \tan^{-1} \left(\frac{U}{Q} \right), \quad (3)$$

and

$$\delta\theta = 0.5 \times \frac{\sqrt{(Q^2 \times \delta U^2 + U^2 \times \delta Q^2)}}{(Q^2 + U^2)} \times \frac{180^\circ}{\pi} \quad (4)$$

The debiased polarized intensity, polarization fraction and angle derived as explained above are used in the analysis of the paper. Magnetic field orientation is derived by rotating the θ by 90° . The details of the procedure followed in producing polarization values is explained in detail by [Kwon et al. \(2018\)](#).

3. RESULTS

Figure 1 shows the Stokes I map of Oph-B obtained from SCUBA-2/POL-2 observations. The Oph-B clump contains two structures, one in the southwest known as Oph-B1 and other in the northeast known as Oph-B2 ([Motte et al., 1998](#)). These structures are labeled with boxes in figure 1. The entire clump appears to be rather

cold, with dust temperatures ranging from ~ 7 to 23 K at the center of the clump ([Stamatellos et al., 2007](#)).

The Oph-B region contains at least three Class I protostars and five flat spectrum objects, many of which are driving outflows ([White et al., 2015](#)). Figure 2 shows the distributions of young stellar objects (YSOs) in Oph-B with the blue- and red-shifted lobes of the molecular outflows driven by IRS 47, as identified by [White et al. \(2015\)](#), marked. Figure 2 also shows dense condensations identified using Gaussclump ([Stutzki & Guesten, 1990](#)) in N_2H^+ (1-0) data by [André et al. \(2007\)](#).

B-fields derived from dust polarization measurements are shown by white line segments in the left-hand panel of figure 3. The polarization vectors are rotated by 90° to show the B-field orientation. The length of the vectors shows the polarization fraction. The underlying image is the Stokes I map, showing the geometry of the cloud. For the following analysis we used those polarization measurements where $\frac{PI}{\delta PI} > 2$ in order to ensure we have a large and robust sample. The measurements with $\frac{PI}{\delta PI} > 3$ are also shown as cyan color vectors in figure 3. PI and δPI are the polarized intensity and uncertainty on polarized intensity, respectively. The B-field orientations obtained from NIR polarization measurements by [Kwon et al. \(2015\)](#) are shown in the figure as red line segments. The right-hand panel of figure 3 shows the B-field orientation, with polarization vectors normalized. Here the lengths of vectors are independent of the polarization fraction.

Figure 4 shows the polarization vectors (rotated by 90°) with the data averaged over four pixels using 2×2 binning, showing the general morphology of the B-fields.

Figure 5 compares the distribution of position angle in Oph-B1 and Oph-B2 using the POL-2 data from figure 3. The figure shows histograms of each complex and of the entire Oph-B clump.

3.1. Comparison of SCUBA-POL and SCUBA-2/POL-2 results

[Matthews et al. \(2009\)](#) cataloged polarization observations for various star-forming regions using $850\mu m$ data obtained using SCUBA-POL (SCUPOL) at the JCMT. Figure 6 compares the polarization vectors (not rotated by 90°) towards Oph-B2 (Oph-B1 was not observed with SCUPOL). We found 27 SCUPOL data points with coordinates which matched to those of our observations within $10''$. The polarization vectors in common agree well in position angles. Figure 7 shows a comparison of degree of polarization and position angle between the two datasets. The polarization angles measured by the two instruments agree with each other within the errors (figure 7 upper panel). In contrast,

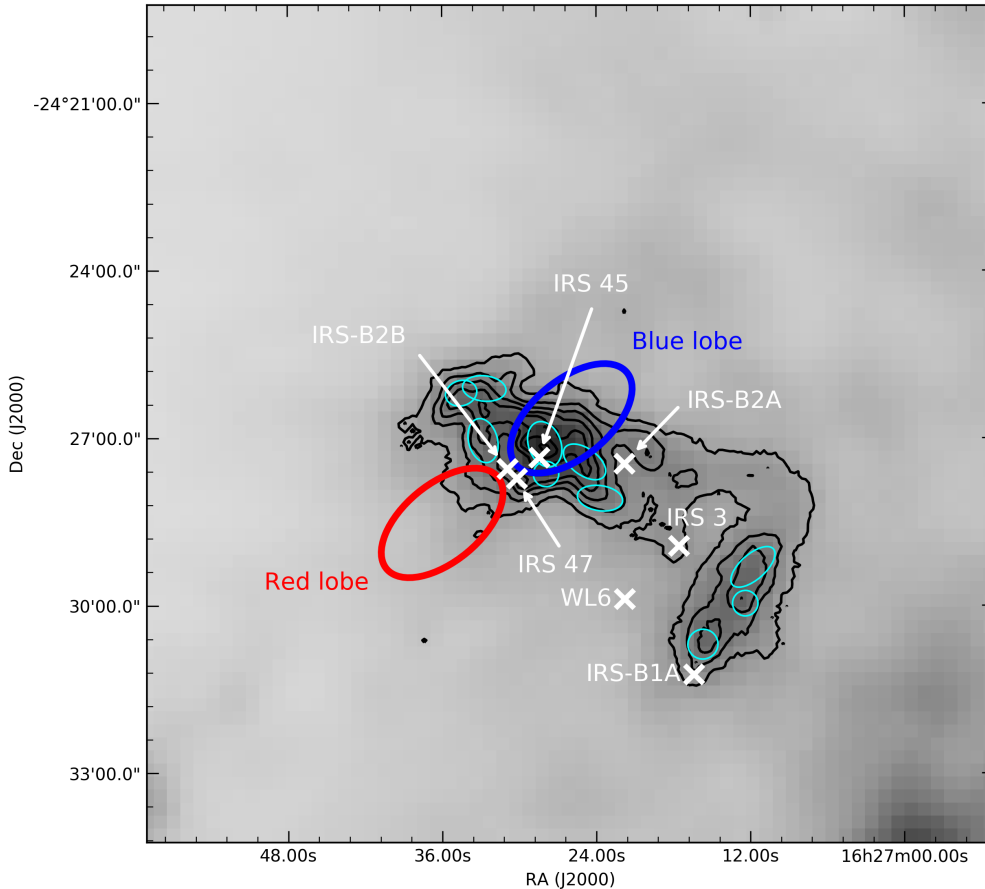


Figure 2. This figure shows submm continuum emission and outflow-related structures and YSO locations in Oph-B. The background image shows Herschel $500\mu\text{m}$ emission. Contours show the $850\mu\text{m}$ SCUBA-2 dust continuum emission. The positions of YSOs identified in the region are marked with white crosses and labeled. Blue and red ellipses show the blue- and red-shifted wings of the prominent outflow associated with IRS47 (White et al., 2015), respectively. Cyan ellipses show the dense structures identified in N_2H^+ data (André et al., 2007). IRS-B1A, IRS-B2A and IRS-B2B correspond to YSOs SSTc2dJ162716.4-243114, SSTc2d162721.8-242728 and SSTc2d162730.9-242733 in the SIMBAD database, respectively.

the polarization fraction measured with SCUPOL are systematically higher than those with POL-2, especially in the low P values data (figure 7 lower panel), suggesting that such a difference is caused by the fact that errors in polarization fraction, P, do not obey Gaussian statistics, since P can never be negative, and hence, as discussed above, absolute values of P observed with all instruments and at all wavelengths tend to increase in areas of very low SNR. This has been discussed in detail by Vaillancourt (2006) placing the confidence level in polarization measurements. The SCUPOL data have lower SNR than our own data, and consequently the polarization fractions measured with that instrument are typically higher than those measured with POL-2.

We also performed the Kolmogorov-Smirnov (K-S; Press et al., 1992) statistical test to quantify the deviation between SCUPOL and POL-2 polarization position angles towards Oph-B2 and found a probability of 0.905. The average difference in the orientation between

the position angles of SCUPOL and POL-2 segments is found to be $\sim 20^\circ$. The distribution of the differences in the orientations of position angles in these two samples peaks at $\sim 10 - 20^\circ$. Detailed quantitative comparison of POL-2 data with SCUPOL is difficult because of the poor number statistics and low SNR in the SCUPOL data. However, we note that the two sets of vectors are broadly consistent, and agree best in the center of the SCUPOL field. Also, note that POL-2 data have much higher sensitivity than SCUPOL, which provide more reliable polarization angles.

4. DISCUSSION

4.1. The magnetic field in NIR wavelengths

Kwon et al. (2015) presented the B-field morphology across Ophiuchus, measured using dust extinction in the

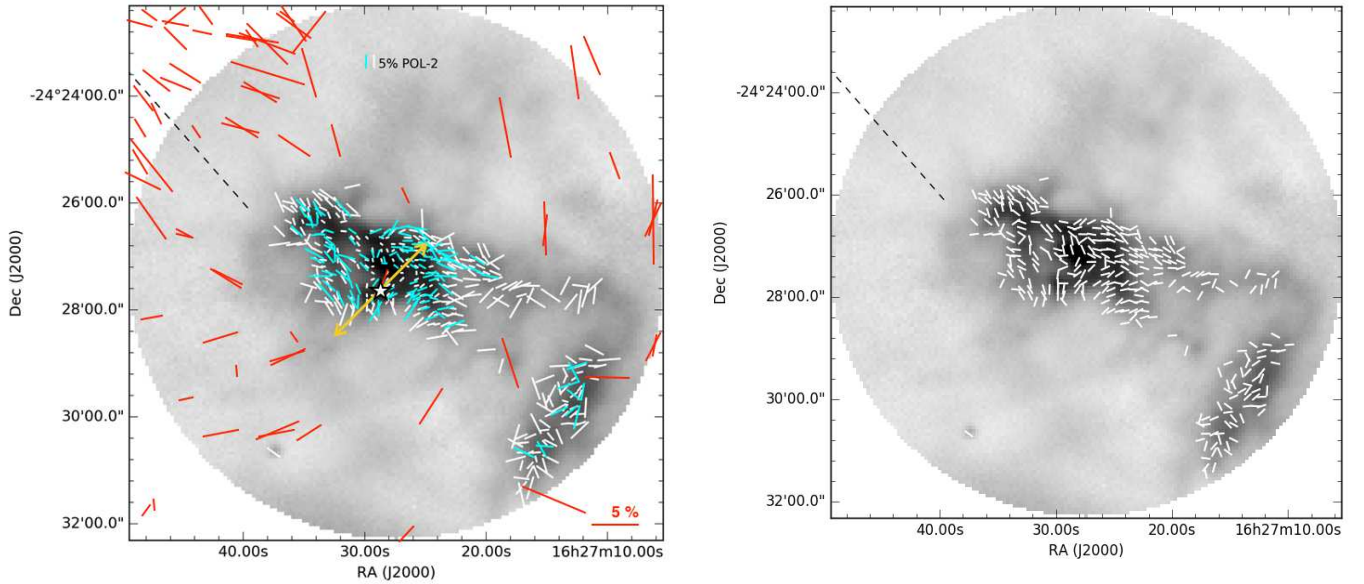


Figure 3. *Left panel:* B-field orientation in Oph-B from $850\mu\text{m}$ dust polarization data. The background image shows the dust continuum map at $850\mu\text{m}$ from SCUBA-2. The white and cyan color vectors correspond to data with $PI/\delta PI > 2$ and $PI/\delta PI > 3$, respectively. The vectors are rotated by 90° to show the inferred B-field morphology. The white star symbol represents the position of IRS47, with its associated bipolar outflow shown using a double-headed arrow in yellow. A 5% polarization vector is shown for reference. The red vectors shows the B-fields mapped using deep NIR observations by (Kwon et al., 2015). The black dashed line shows the orientation of the Galactic Plane at the latitude of the cloud. *Right panel:* Same as left panel (except NIR data), but the vectors are of uniform length, rather than scaled with polarization fraction.

J, H and K bands using SIRPOL¹. Near-infrared (NIR) polarimetry can probe B-fields in diffuse environments ($A_V \sim 10 - 20$ mag; Tamura 1999; Tamura et al. 2011). However, these data cannot probe the high-density regions where stars themselves form. To study the B-field morphology on $\lesssim 1$ pc scales, Kwon et al. (2015) compared the NIR data with optical polarimetry data tracing B-fields on 1-10 pc scales in the Ophiuchus region (Vrba et al., 1976). Their investigation suggested that the B-field structures in the Ophiuchus clumps were distorted by the cluster formation in this region, which may have been induced by a shock compression by winds and/or radiation from the Scorpius–Centaurus association towards its west. The overall B-field observed at NIR wavelengths is found to have an orientation of 50° East of North (Kwon et al., 2015).

4.2. The magnetic field morphology in submm wavelengths

Submm polarimetry probes B-fields in relatively dense ($A_V \sim 50$ mag) regions of clouds. It can be noticed in

figure 5 that the distribution of position angles peaks at $\theta = 50-80^\circ$, suggesting that the large-scale B-field is a dominant component of the cloud’s B-field geometry. There is a more clearly prevailing B-field orientation in Oph-B2, as demonstrated by the peak in the distribution shown in the histogram. The 1000-2000 AU-scale B-field traced by $850\mu\text{m}$ polarimetry seems to follow the structure of the two clumps, if we consider the field geometry as a whole. In figure 3, it is clear that a B-field component with an orientation of $50-80^\circ$ is present in the low-density periphery of the cloud, and seems to be connecting well to the large-scale B-fields revealed at NIR wavelengths (shown as red vectors in the figure). This component is also present in Planck polarization observations (Planck Collaboration et al., 2015). This orientation is also supported by the position angle of a single isolated detection in the south-east of the Oph-B region, which has a position angle $\sim 60^\circ$. The mean magnetic field direction in Oph-B2 by Gaussian fitting to the position angles is measured to be $78 \pm 40^\circ$. The position angle of Oph-B2 major axis is found to be 60° inferred by fitting an ellipse to the clump. The angular offset between the mean B-field direction and the major axis of Oph-B2 suggests that the B-field is con-

¹ SIRIUS camera in POLarimeter mode on the IRSF 1.4 m telescope in South Africa (Kandori et al., 2006)

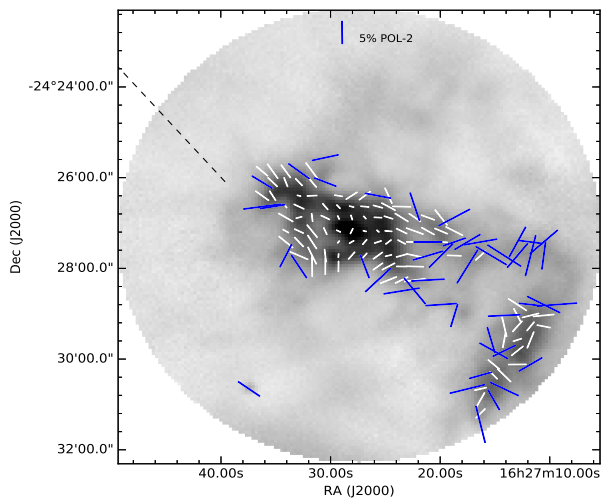


Figure 4. Smoothed B-field orientations in Oph-B, shown on the $850\mu\text{m}$ dust emission map from SCUBA-2. The polarization data are averaged over 4 pixels (an effective pixel size of $8''$ using 2×2 binning). White vectors correspond to data with $P < 5\%$, while blue vectors correspond to data with $P > 5\%$. The vectors are selected to have $PI/\delta PI > 2$, and are rotated by 90° to show the inferred B-field morphology. A reference vector with 5% polarization is given for scale. The black dashed line shows the orientation of the Galactic Plane at the latitude of the cloud.

sistent with a field that is parallel both to the long axis of Oph B2, and to the filament-like structure in which it lies. The diffuse filamentary structure connecting the two clumps seems to have B-field lines orthogonal to it. This can be seen from the overall geometry of the B-field lines in this low-density region, which follows the clump structures. We more clearly show the smoothed B-field geometry in figure 4. In this figure, the B-field vectors corresponding to $P > 5\%$ and $P < 5\%$ are plotted in blue and white, respectively. The overall B-field geometry seems somewhat disordered (see section 4.4), with the blue vectors showing a higher degree of polarization towards the more diffuse parts of the cloud, and the white vectors showing the B-fields in the dense core regions.

4.3. Variation of polarization fraction

The left-hand panel in figure 8 shows a map of polarization intensity towards Oph-B, with contours of Stokes I emission overlaid. The figure shows a decrease in polarization fraction in denser regions (as traced by the Stokes I emission). This depolarization has also been seen in many previous studies (e.g. Dotson, 1996; Matthews & Wilson, 2002; Girart et al., 2006; Tang et al., 2009a,b, 2013). It is noticed that the

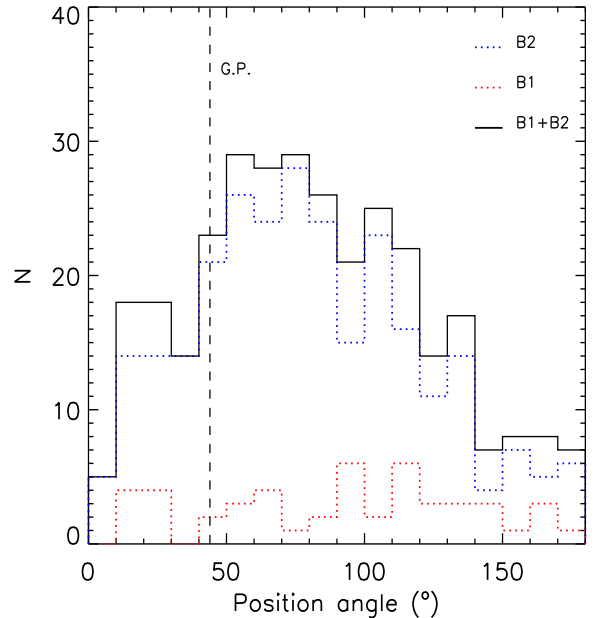


Figure 5. Distributions of position angles (after 90° rotation) corresponding to data with $PI/\delta PI > 2$ shown as white vectors in figure 3. Histograms are shown for Oph-B1 in red, Oph-B2 in blue, and the entire Oph-B clump in black. The bin size is 10° for each distribution. The dashed line represents the orientation of the Galactic Plane.

polarization fraction is relatively higher on the edges of the cloud than in the denser core regions (see figure 4). Plausible causes for the polarization fraction hole effect have been discussed in previous studies, such as Hull et al. (2014). They found that in low-resolution maps (i.e. $\sim 20''$ resolution, obtained from SHARP², Hertz and SCUBA), depolarization resulted from unresolved structure being averaged across the beam. However, in high-resolution maps (i.e. $\sim 2.5''$ resolution, obtained using CARMA³), depolarization persisted even after resolving the twisted plane-of-sky B-field morphologies.

Except for a very few lines of sight through the densest parts of protostellar disks, (sub)millimeter-wavelength thermal dust emission is optically thin. Therefore, polarization data at these wavelengths will be an integration of the emission along the entire line of sight. If the B-field changes along the line of sight (e.g. due to turbulence), the observed dust polarization will be averaged, and so will result in a lower observed polarization fraction. Future higher-resolution ALMA observations can

² The SHARC-II polarimeter for CSO

³ Combined Array for Research in Millimeter Astronomy

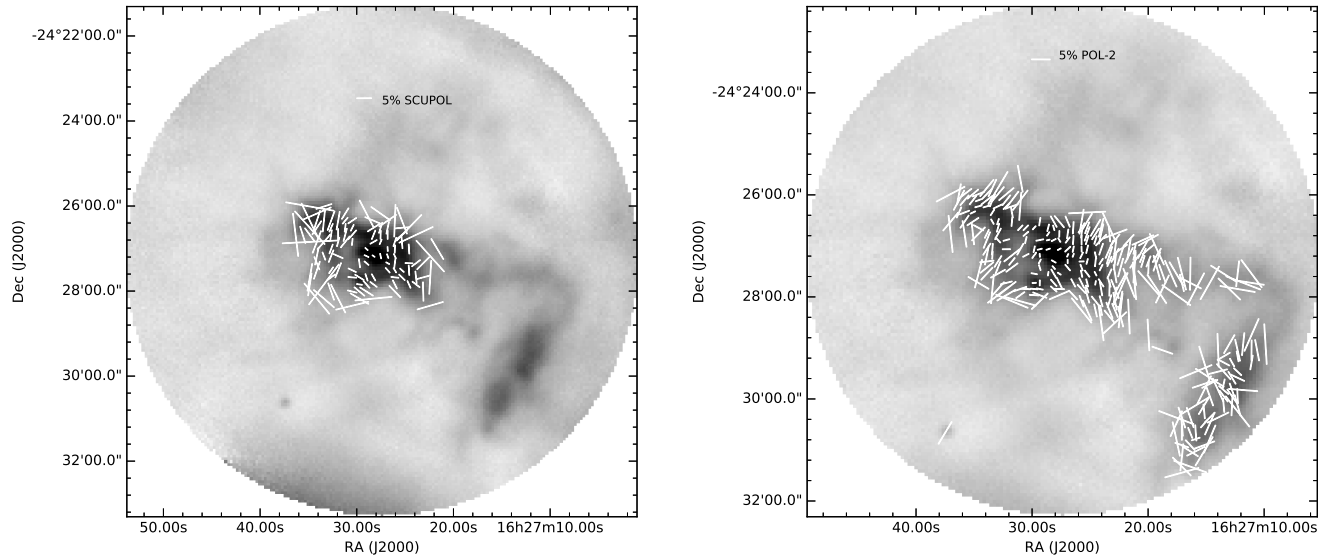


Figure 6. A comparison between SCUPOL (left panel) data (Matthews et al., 2009) and SCUBA-2/POL-2 (right panel) data (this work), both taken at the JCMT at $850\mu\text{m}$. These are unrotated polarization vectors not B-fields orientations.

help in tracing the magnetic field structure at different scales in the cloud (e.g., Hull et al., 2013, 2014).

The polarization hole effect has also been explained as resulting from different grain characteristics in dense cores than in diffuse regions. Grain growth can make grains more spherical and thus harder to align with B-fields by radiative torques. Grain alignment can also be disturbed due to collisions in the higher density regions resulting in low polarization.

Alternatively the polarization hole effect could arise from a loss of photon flux to drive grain alignment in very dense regions. According to modern grain alignment theory, dust grains are aligned by radiative torques (Lazarian & Hoang, 2007; Hoang & Lazarian, 2008, 2009, 2016). Towards a dense region, the magnitude of these Radiative Alignment Torques (RATs) decreases due to the attenuation of the interstellar radiation. As a result, grain alignment may be suppressed in very high extinction regions, resulting in a decrease in the observed fractional polarization.

Wolf et al. (2003) found that the polarization fraction in molecular clouds follows the relation $P \propto I^{-\alpha}$, with $\alpha \sim 0.5 - 1.2$. They also reported a value of α of -0.43 towards some Bok globules. Arce et al. (1998) observed a similar behavior in the dust extinction polarization of background starlight. Falceta-Gonçalves et al. (2008) performed a statistical investigation of the previous studies in order to understand this trend. They produced synthetic polarimetric maps and found an anti-

correlation between polarization degree and column density with a value of α of -0.5 (assuming perfect grain alignment with no dependence on extinction), due to an increase in the dispersion of the polarization angle along the line of sight in the denser regions. Cho & Lazarian (2005), in their study of grain alignment, claimed that power law index is sensitive to the grain size distribution.

Measured values of α can vary in different cases. For example, Matthews & Wilson (2000) found a relation of $P \propto I^{-0.7}$ towards OMC-3, but $P \propto I^{-0.8}$ in the Barnard 1 cloud. In the case of dense star-forming cores, Henning et al. (2001) measured $P \propto I^{-0.6}$, whereas Lai et al. (2002) found $P \propto I^{-0.8}$, and Crutcher (2004) obtained a slightly steeper value of α , with $P \propto I^{-1.2}$. The relationship between polarization fraction and intensity may be different in dense cores. Hull et al. (2017b) found a relatively high polarization fraction near the total intensity peak of Serpens SMM1 using ALMA data. This higher degree of polarization may possibly be due to additional radiative torques from its young central protostar.

The right-hand panel of figure 8 compares degree of polarization with $850\mu\text{m}$ dust emission intensity in Oph-B. We measured the power-law slope in the distribution using a least-squares fit, and found $\alpha \approx -0.9$. A similar value has been reported by Alves et al. (2014) towards starless cores. Most recent ALMA observations at $0.26''$ resolution towards W51 e2, e8, North show a slope of

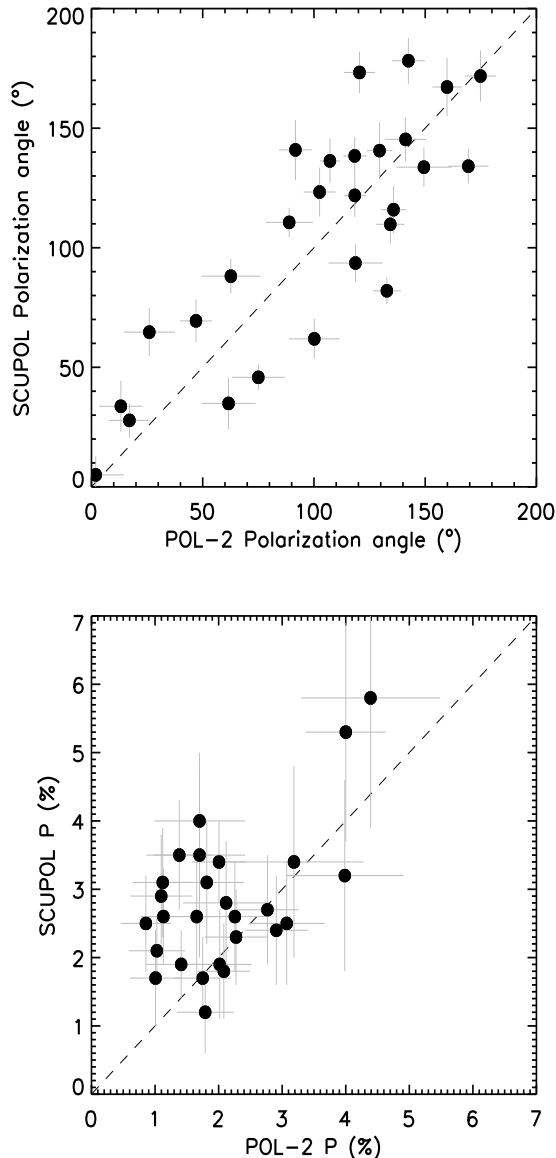


Figure 7. A comparison of polarization angle (top) and fraction (bottom) values obtained towards Oph-B2 by SCUPOL (Matthews et al., 2009) and SCUBA-2/POL-2 (this work). Dashed lines show a one-to-one relation (see text for details).

-0.84 to -1.02 and SMA observations at $2''$ resolution towards the same source in e2/e8 and North reported a slope of -0.9 and -0.86, respectively (Koch et al., 2018). Higher-resolution polarization observations (i.e. using ALMA) are needed to probe the magnetic fields toward the very centers of the embedded cores in Oph-B, on the scales < 1000 AU.

4.4. The Davis-Chandrasekhar-Fermi analysis for B-field strength

We use the Davis-Chandrasekhar-Fermi (DCF; Davis 1951; Chandrasekhar & Fermi 1953) method to estimate the plane-of-sky magnetic field strength in Oph-B. This method assumes that the underlying magnetic field geometry of the region under consideration is uniform, and hence that the observed dispersion in position angle is a measure of the distortion in the field geometry caused by turbulence, and also that the distribution of vectors about the mean field direction is approximately Gaussian, and thus well-characterized by its standard deviation.

The DCF method estimates the plane-of-sky B-field (B_{pos}) using the formula

$$B_{pos} = Q\sqrt{4\pi\rho}\frac{\sigma_v}{\sigma_\theta}, \quad (5)$$

where ρ is the gas density, σ_v is the 1D non-thermal velocity dispersion of the gas, σ_θ is the dispersion in polarization angle, and Q is a factor of order unity that accounts for variations in the B-field on scales smaller than the beam.

Crutcher (2004) formulated this as:

$$B_{pos} \approx 9.3\sqrt{n(\text{H}_2)}\frac{\Delta v}{\sigma_\theta} \mu\text{G}, \quad (6)$$

where $n(\text{H}_2)$ is the number density of molecular hydrogen in cm^{-3} , $\Delta v = \sigma_v\sqrt{8\ln 2}$ in km s^{-1} , σ_θ is in degrees, and Q is taken to be 0.5 (cf. Ostriker et al. 2001).

4.4.1. Number density

Motte et al. (1998) infer a volume density in Oph-B of $n(\text{H}_2) = 3.2 \times 10^6 \text{ cm}^{-3}$ from 1.3 mm dust continuum measurements. We adopt this value throughout the subsequent analysis. These authors estimate that their measured column densities are accurate to within a factor $\lesssim 2$, so we conservatively adopt a fractional uncertainty of $\pm 50\%$ on their stated volume density.

4.4.2. Velocity dispersion

André et al. (2007) observed Oph-B in the N_2H^+ $J = 1 \rightarrow 0$ line with beam size $26''$ using IRAM 30m telescope. Pattle et al. (2015) showed that there is good agreement between core masses derived using these N_2H^+ data and core masses derived using SCUBA-2 $850\mu\text{m}$ continuum observations of Oph-B (see their figure 8). Hence, we assume that N_2H^+ traces the same density region as our SCUBA-2/POL-2 observations do, and so that the non-thermal velocity dispersions measured by André et al. (2007) are representative of the non-thermal motions perturbing the magnetic field which we observe in Oph-B.

André et al. (2007) list non-thermal velocity dispersion for 19 of the cores in Oph-B2 identified by

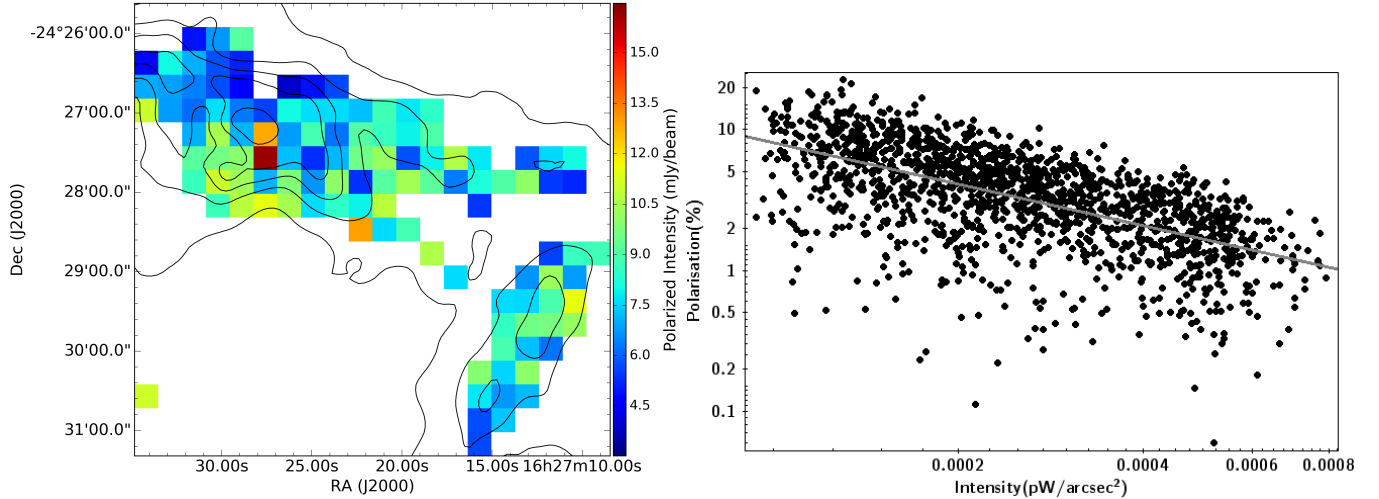


Figure 8. Left panel shows the map of polarization intensity with dust continuum contour overlaid. The degree of polarization vs. total intensity plot is shown in right panel after selecting the sample using $I > 0$, $\frac{I}{\delta I} > 20$, and $P > 0$. The grey line shows the linear fitting in the data.

Motte et al. (1998) in their Table 4 (note that we use the non-background-subtracted values in order to have the best possible correspondence with the integrated dust column). Averaging these velocity dispersion, we estimate $\sigma_v = 0.24 \pm 0.08 \text{ km s}^{-1}$, i.e. $\Delta v = 0.56 \pm 0.20 \text{ km s}^{-1}$, where the uncertainties give the standard deviation on the mean.

4.4.3. Angular dispersion

To ensure that we are measuring the dispersion of statistically independent pixels, and to maximize the fraction of the map with high SNR measurements, we gridded the vector map to $12''$ (approximately beam-sized) pixels. We performed the DCF analysis on Oph-B2 only, because the field in Oph-B1 is quite disordered, as seen in figure 5, with no clear peak in the distribution of angles. The DCF method thus cannot be meaningfully applied in this region.

There are many methods of estimating the angular dispersion in polarization maps. The polarization vectors in Oph-B2 show a relatively ordered morphology with some scatter along the edges. Naively taking the standard deviation of all pixels in Oph-B2 with $PI/\delta PI > 2$, we measure $\sigma_\theta = 42^\circ$. This value is significantly larger than the maximum value at which the standard DCF method can be safely applied ($\lesssim 25^\circ$; Heitsch et al. 2001). This large standard deviation includes both the scatter in polarization vectors and any underlying variations in the ordered field.

Instead, we followed the technique to measure the dispersion of polarization angle presented by Pattle et al. (2017). They used an unsharp-masking method to remove the underlying ordered magnetic field structure from their observations. Firstly, they estimated the gen-

eral magnetic field structure by smoothing their map of magnetic field with a 3×3 -pixel boxcar filter. Secondly, they subtracted the smoothed map from the observed magnetic field angle map. The resulting residual map was taken to represent the non-ordered component of the magnetic field. Finally, they used the standard deviation in the residual map to represent the standard deviation in the magnetic field angle, σ_θ . We refer readers to Pattle et al. (2017) for a detailed description of the methodology.

We applied the Pattle et al. (2017) method to our Oph-B2 data. Figure 9 shows the observed projected magnetic field (left panel), the inferred ordered component to the field (middle panel), and the residual map (right panel). We restrict our analysis to pixels where $P/\delta P > 3$ (although the SNR may be lower in the surrounding pixels, which contribute to the mean field estimate), and exclude any pixel where the maximum difference in angle between pixels within the boxcar filter is ≥ 90 degrees, on the assumption that the field in the vicinity of that pixel is not sufficiently uniform for the smoothing function to be valid. We measure a standard deviation in the residual map of $\sigma_\theta = 14.8^\circ \pm 0.7^\circ$, as shown in figure 10.

The method proposed by Pattle et al. (2017) was developed for data with higher SNR than we achieve in Oph-B. We tested the accuracy of this estimate of σ_θ by measuring the standard deviation in angle in small regions of Oph-B2 which do not show significant ordered variation across them. We measured $\sigma_\theta = 12.8^\circ$ in the north-west of Oph-B2, $\sigma_\theta = 16.6^\circ$ in the north-east, and $\sigma_\theta = 16.5^\circ$ in the south-west. This suggests that the dispersion in angle that we measure using the unsharp

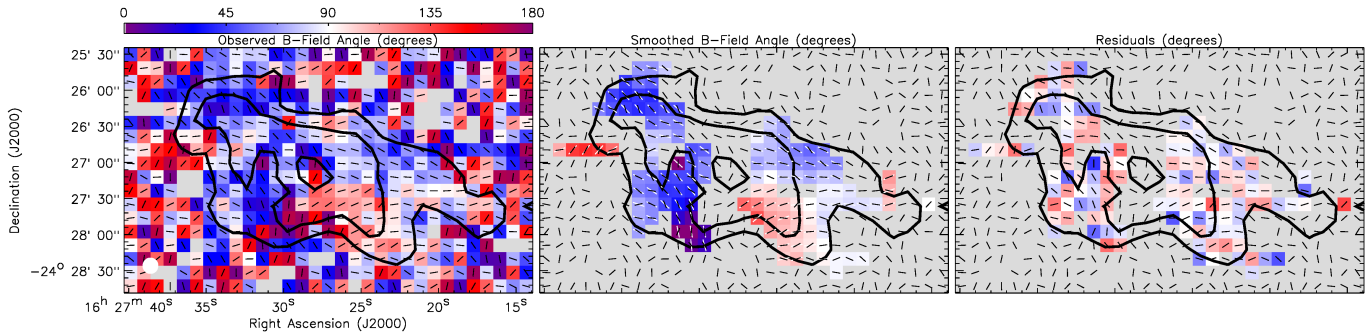


Figure 9. Left panel: The observed magnetic field angles in Oph-B2. Middle panel: The magnetic field angle map smoothed with a 3×3 -pixel boxcar filter. Right panel: The residual map from subtracting the smoothed map from the observations. Contours show Stokes I emission at 1.0, 2.0 and 3.0 mJy/arcsec^2

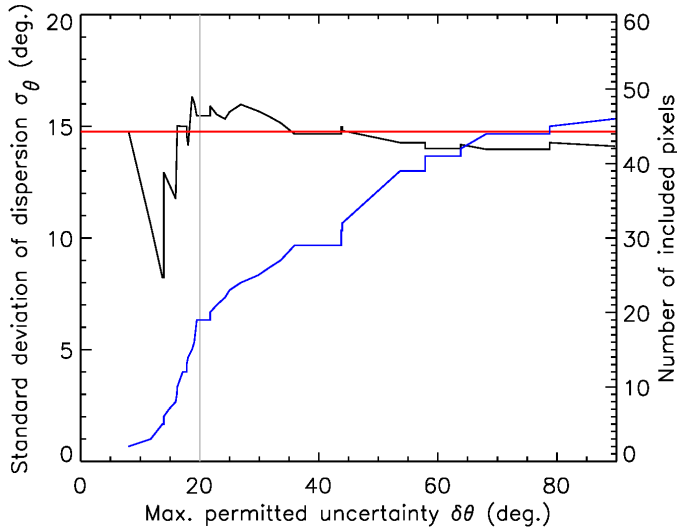


Figure 10. Black line: the standard deviation (σ_θ), of the distribution of the magnetic field angles in Oph-B2 about the mean magnetic field direction as a cumulative function of maximum uncertainty in the 3×3 -pixel smoothing box (left-hand axis). Red line: the mean value of standard deviation, measured over the distribution to the right of the grey line (left-hand axis). Blue line: the number of pixels included in the cumulative distribution (right-hand axis).

masking method is representative of the true dispersion in angle may be due to non-thermal motions in Oph-B2, and so we adopt $\sigma_\theta \sim 15^\circ$ going forward.

4.4.4. Magnetic field strength

Using our values of $n(\text{H}_2) = (3.2 \pm 1.6) \times 10^6 \text{ cm}^{-3}$, $\Delta v = 0.56 \pm 0.20 \text{ km s}^{-1}$ and $\sigma_\theta = 14.8 \pm 0.7^\circ$, we estimate a plane-of-sky magnetic field strength in Oph-B2 of $630 \mu\text{G}$. Combining our uncertainties using the relation

$$\frac{\delta B_{pos}}{B_{pos}} = \frac{1}{2} \frac{\delta n(\text{H}_2)}{n(\text{H}_2)} + \frac{\delta \Delta v}{\Delta v} + \frac{\delta \sigma_\theta}{\sigma_\theta}, \quad (7)$$

where $\delta n(\text{H}_2)$ represents the uncertainty on $n(\text{H}_2)$ and so forth, we find a total fractional uncertainty of

$\delta B_{pos}/B_{pos} \approx 66\%$. We note that a significant fraction of the contribution to this uncertainty is systematic, and thus that our result of $B_{\text{sky}} = 630 \pm 410 \mu\text{G}$ suggests that the magnetic field strength in Oph-B2 is possibly within the range $200 - 1000 \mu\text{G}$.

4.4.5. Small-angle approximation

The DCF method fails at large angular dispersions in part due to the failure of the small-angle approximation, as discussed in detail by Heitsch et al. (2001) and Falceta-Gonçalves et al. (2008). For our measured value of angular dispersion, $\sigma_\theta = 15^\circ = 0.262$ radians, $\tan(\sigma_\theta) = 0.268$, i.e. $\tan(\sigma_\theta)/\sigma_\theta = 1.02$. We are in the regime in which the small-angle approximation holds well, and so the standard DCF method is an appropriate choice here.

4.4.6. Line-of-sight turbulence

Many authors have discussed the appropriate value of the Q parameter in the DCF equation to properly account for variations if the magnetic field along the line of sight or field on scales smaller than the beam (e.g. Ostriker et al. 2001; Heitsch et al. 2001; Houde et al. 2009; Cho & Yoo 2016). Modeling suggests that the DCF method will overestimate the magnetic field strength by a factor of \sqrt{N} , where N is the number of turbulent eddies along the line of sight (Heitsch et al., 2001). Cho & Yoo (2016) propose that the number of turbulent eddies can be estimated using the relation

$$\frac{1}{\sqrt{N}} \sim \frac{\sigma_{v_c}}{\sigma_v}, \quad (8)$$

where σ_{v_c} is the standard deviation in the centroid velocities across the observed region, and σ_v is the average line-of-sight non-thermal velocity dispersion, as previously discussed.

Using the centroid velocities listed in Table 2 of André et al. (2007), we estimate $\sigma_{v_c} = 0.218 \text{ km s}^{-1}$, for the same 19 cores as were used to estimate σ_v . Thus,

we find that $\sigma_{V_c}/\sigma_v = 0.915$, i.e. $N \sim 1$. Thus we do not expect large numbers of turbulent eddies along the line of sight, and so any over-estimation of the magnetic field in Oph-B2 due to this effect should be minimal.

4.4.7. Mass-to-flux ratio

The relative importance of gravity and B-fields to the overall stability of a region is represented by the mass-to-flux ratio, λ (Crutcher, 2004). The stability of cores can be estimated observationally using H_2 column density and B-field strength. We assume that the average field strength from the larger Oph-B2 region applies to the dense cores within the region. Motte et al. (1998) estimated the column density of Oph-B2 to be $41 \times 10^{22} \text{cm}^{-2}$. Thus, its mass-to-flux stability parameter, λ , can be estimated using the relation given by Crutcher (2004),

$$\lambda = 7.6 \times 10^{-21} \frac{N(H_2)}{B_{\text{pos}}}, \quad (9)$$

where $N(H_2)$ is the molecular hydrogen column density in cm^{-2} and B_{pos} is the plane-of-the sky field strength in μG . From our values of B_{pos} (see Section 4.4) and $N(H_2)$, we find $\lambda = 4.9 \pm 3.2$ where the error comes from the uncertainty in B-field strength measurement only. According to Crutcher (2004) this value can be overestimated by a factor of 3 due to geometric effects. Thus, the corrected value of λ is 1.6 ± 1.1 , which is treated as the lower limit of λ in this work. A value of $\lambda > 1$ indicates that the core is magnetically supercritical, suggesting that its B-field is not sufficiently strong to prevent gravitational collapse. The values of λ estimated towards Oph-B2 suggest that this clump is slightly magnetically supercritical.

4.5. Relative orientation between outflows and magnetic fields

Hull et al. (2014) used CARMA observations to investigate the relationship between outflow directions and B-field morphologies in a large sample of young star-forming systems. They found that their sample was consistent with random alignments between B-fields and outflows. Nevertheless, sources with low polarization fractions (similar to Oph-B2) appear to have a slight preference for misalignment between B-field directions and outflow axes, suggesting that their field lines are wrapping around the outflow due to envelope rotation.

Oph-B2 contains a prominent outflow driven by IRS47 (White et al., 2015). The plane-of-sky position angle of outflow is $\sim 140^\circ$, which is roughly 50° offset from the general orientation of the B-field in the vicinity of the outflow. The offset between the overall B-field orientation in Oph-B2 ($\sim 80^\circ$) and the outflow from IRS47

is $\sim 60^\circ$. These results suggest that outflows are not aligned with the B-field in Oph-B on the size scales that we observe. This is consistent with models which suggest outflows are misaligned to magnetic field orientation (Hennebelle & Ciardi, 2009; Joos et al., 2012; Li et al., 2013).

5. SUMMARY

This paper presents the first-look results of SCUBA-2/POL-2 observations in the $850\mu\text{m}$ waveband towards the Oph-B region by the BISTRO survey. In this study, we mainly focused on the role of B-fields in star formation. The main findings of this work are summarized below:

1. We found polarization fractions and angles to be consistent with previous SCUPOL data. But our POL-2 map is more sensitive than the archival data and covers a larger area of the Oph-B clump.
2. We identify distinct magnetic field morphologies for the two sub-clumps in the region, Oph-B1 and Oph-B2. Oph-B1 appears to be consistent with having a random magnetic field morphology on the scales which we observe, whereas Oph-B2 shows an underlying ordered field in its denser interior.
3. The field in Oph-B2 is relatively well-ordered and lies roughly parallel ($\sim 18^\circ$) to the long axis of the clump.
4. We find that the B-field component lying on the low density periphery of the Oph-B2 clump is parallel to the large-scale B-field orientation identified in previous studies using observations made at NIR wavelengths. The sub-mm data show detailed structure that could not be detected with the NIR data.
5. The decrease in the polarization fraction is observed in the densest regions of both Oph-B1 and B2.
6. We measured the magnetic field strength in Oph-B2 using the Davis-Chandrasekhar-Fermi (DCF) method. Since this sub-clump has an underlying ordered field structure, we used an unsharp-masking technique to obtain an angular dispersion of $\sim 15^\circ$. We measured a field strength of $630 \pm 410 \mu\text{G}$ and a mass-to-flux ratio of 1.6 ± 1.1 , suggesting that Oph-B2 is slightly magnetically supercritical.
7. We examined the relative orientation of the most prominent outflow in Oph-B2 (IRS 47) and the

local magnetic field. The two have orientations that are offset by $\sim 50^\circ$, suggesting they are not aligned. The angular offset between the large-scale magnetic field in Oph-B2 and the outflow orientation is $\sim 60^\circ$, suggesting consistency with models which predict that outflows should be misaligned to magnetic field direction.

6. ACKNOWLEDGMENTS

Authors thank referee for a constructive report that helped in improving the content of this paper. The James Clerk Maxwell Telescope is operated by the East Asian Observatory on behalf of the National Astronomical Observatory of Japan, the Academia Sinica Institute of Astronomy and Astrophysics, the Korea Astronomy and Space Science Institute, the National Astronomical Observatories of China and the Chinese Academy of Sciences (Grant No. XDB09000000), with additional funding support from the Science and Technology Facilities Council of the United Kingdom and participating universities in the United Kingdom and Canada. The James Clerk Maxwell Telescope has historically been operated by the Joint Astronomy Centre on behalf of the Science and Technology Facilities Council of the United Kingdom, the National Research Council of Canada and the Netherlands Organisation for Scientific Research. Additional funds for the construction of SCUBA-2 and POL-2 were provided by the Canada Foundation for Innovation. The data used in this paper were taken under project code M16AL004. AS would like to acknowledge the support from KASI for postdoctoral fellowship. K.P. acknowledges support from the Science and Technology Facilities Council (STFC) under grant number ST/M000877/1 and the Ministry of Science and

Technology, Taiwan, under grant number 106-2119-M-007-021-MY3, and was an International Research Fellow of the Japan Society for the Promotion of Science for part of the duration of this project. CWL and MK were supported by Basic Science Research Program through the National Research Foundation of Korea (NRF) funded by the Ministry of Education, Science and Technology (CWL: NRF-2016R1A2B4012593) and the Ministry of Science, ICT & Future Planning (MK: NRF-2015R1C1A1A01052160). W.K. was supported by Basic Science Research Program through the National Research Foundation of Korea (NRF-2016R1C1B2013642). JEL is supported by the Basic Science Research Program through the National Research Foundation of Korea (grant No. NRF-2018R1A2B6003423) and the Korea Astronomy and Space Science Institute under the R&D program supervised by the Ministry of Science, ICT and Future Planning. D.L. is supported by NSFC No. 11725313. S.P.L. acknowledges support from the Ministry of Science and Technology of Taiwan with Grant MOST 106-2119-M-007-021-MY3. K.Q. acknowledges the support from National Natural Science Foundation of China (NSFC) through grants NSFC 11473011 and NSFC 11590781. This research has made use of the NASA Astrophysics Data System. AS thanks Maheswar G. for discussion on polarization in star-forming regions. AS also thanks Piyush Bhardwaj (GIST, South Korea) for a critical reading of the paper. The authors wish to recognize and acknowledge the very significant cultural role that the summit of Maunakea has always had within the indigenous Hawaiian community, with reverence. AS specially thanks the JCMT TSS for the hard-earned data.

REFERENCES

- Allen, A., Li, Z.-Y., & Shu, F. H. 2003, *ApJ*, 599, 363
- Alves, F. O., Frau, P., Girart, J. M., et al. 2014, *A&A*, 569, L1
- Andersson, B.-G., Lazarian, A., & Vaillancourt, J. E. 2015, *ARA&A*, 53, 501
- André, P., Belloche, A., Motte, F., & Peretto, N. 2007, *A&A*, 472, 519
- Arce, H. G., Goodman, A. A., Bastien, P., Manset, N., & Sumner, M. 1998, *ApJL*, 499, L93
- Attard, M., Houde, M., Novak, G., et al. 2009, *ApJ*, 702, 1584
- Chandrasekhar, S., & Fermi, E. 1953, *ApJ*, 118, 113
- Chapin, E. L., Berry, D. S., Gibb, A. G., et al. 2013, *MNRAS*, 430, 2545
- Chini, R. 1981, *A&A*, 99, 346
- Cho, J., & Lazarian, A. 2005, *ApJ*, 631, 361
- Cho, J., & Yoo, H. 2016, *ApJ*, 821, 21
- Crutcher, R. M. 2004, *Ap&SS*, 292, 225
- Cudlip, W., Furniss, I., King, K. J., & Jennings, R. E. 1982, *MNRAS*, 200, 1169
- Currie, M. J., Berry, D. S., Jenness, T., et al. 2014, in *Astronomical Society of the Pacific Conference Series*, Vol. 485, *Astronomical Data Analysis Software and Systems XXIII*, ed. N. Manset & P. Forshay, 391
- Davis, L. 1951, *Phys. Rev.*, 81, 890.
<https://link.aps.org/doi/10.1103/PhysRev.81.890.2>
- de Geus, E. J., de Zeeuw, P. T., & Lub, J. 1989, *A&A*, 216, 44

- Dib, S., Hennebelle, P., Pineda, J. E., et al. 2010, *ApJ*, 723, 425
- Dib, S., Kim, J., Vázquez-Semadeni, E., Burkert, A., & Shadmehri, M. 2007, *ApJ*, 661, 262
- Dolginov, A. Z., & Mitrofanov, I. G. 1976, *Ap&SS*, 43, 291
- Dotson, J. L. 1996, *ApJ*, 470, 566
- Dotson, J. L., Davidson, J., Dowell, C. D., Schleuning, D. A., & Hildebrand, R. H. 2000, *ApJS*, 128, 335
- Dotson, J. L., Vaillancourt, J. E., Kirby, L., et al. 2010, *ApJS*, 186, 406
- Falceta-Gonçalves, D., Lazarian, A., & Kowal, G. 2008, *ApJ*, 679, 537
- Fiedler, R. A., & Mouschovias, T. C. 1993, *ApJ*, 415, 680
- Friberg, P., Bastien, P., Berry, D., et al. 2016, in *Proc. SPIE*, Vol. 9914, Millimeter, Submillimeter, and Far-Infrared Detectors and Instrumentation for Astronomy VIII, 991403
- Galli, D., & Shu, F. H. 1993, *ApJ*, 417, 243
- Girart, J. M., Rao, R., & Marrone, D. P. 2006, *Science*, 313, 812
- Hall, J. S. 1949, *Science*, 109, 166
- Heitsch, F., Zweibel, E. G., Mac Low, M.-M., Li, P., & Norman, M. L. 2001, *ApJ*, 561, 800
- Hennebelle, P., & Ciardi, A. 2009, *A&A*, 506, L29
- Henning, T., Wolf, S., Launhardt, R., & Waters, R. 2001, *ApJ*, 561, 871
- Hildebrand, R. H. 1988, *QJRAS*, 29, 327
- Hildebrand, R. H., Dragovan, M., & Novak, G. 1984, *ApJL*, 284, L51
- Hiltner, W. A. 1949a, *ApJ*, 109, 471
- . 1949b, *Science*, 109, 165
- Hoang, T., & Lazarian, A. 2008, *MNRAS*, 388, 117
- . 2009, *ApJ*, 697, 1316
- . 2014, *MNRAS*, 438, 680
- . 2016, *ApJ*, 831, 159
- Hoang, T., Lazarian, A., & Andersson, B.-G. 2015, *MNRAS*, 448, 1178
- Holland, W. S., Bintley, D., Chapin, E. L., et al. 2013, *MNRAS*, 430, 2513
- Houde, M., Vaillancourt, J. E., Hildebrand, R. H., Chitsazzadeh, S., & Kirby, L. 2009, *ApJ*, 706, 1504
- Hull, C. L. H., Plambeck, R. L., Bolatto, A. D., et al. 2013, *ApJ*, 768, 159
- Hull, C. L. H., Plambeck, R. L., Kwon, W., et al. 2014, *ApJS*, 213, 13
- Hull, C. L. H., Mocz, P., Burkhart, B., et al. 2017a, *ApJL*, 842, L9
- Hull, C. L. H., Girart, J. M., Tychoniec, L., et al. 2017b, *ApJ*, 847, 92
- Jenness, T., Chapin, E. L., Berry, D. S., et al. 2013, SMURF: SubMillimeter User Reduction Facility, Astrophysics Source Code Library, , ascl:1310.007
- Johnstone, D., Wilson, C. D., Moriarty-Schieven, G., et al. 2000, *ApJ*, 545, 327
- Joos, M., Hennebelle, P., & Ciardi, A. 2012, *A&A*, 543, A128
- Kandori, R., Kusakabe, N., Tamura, M., et al. 2006, in *Proc. SPIE*, Vol. 6269, Society of Photo-Optical Instrumentation Engineers (SPIE) Conference Series, 626951
- Knude, J., & Hog, E. 1998, *A&A*, 338, 897
- Koch, P. M., Tang, Y.-W., Ho, P. T. P., et al. 2018, *ApJ*, 855, 39
- Kwon, J., Tamura, M., Hough, J. H., et al. 2015, *ApJS*, 220, 17
- Kwon, J., Doi, Y., Tamura, M., et al. 2018, *ArXiv e-prints*, arXiv:1804.09313
- Lai, S.-P., Crutcher, R. M., Girart, J. M., & Rao, R. 2002, *ApJ*, 566, 925
- Lazarian, A. 2000, in *Astronomical Society of the Pacific Conference Series*, Vol. 215, Cosmic Evolution and Galaxy Formation: Structure, Interactions, and Feedback, ed. J. Franco, L. Terlevich, O. López-Cruz, & I. Aretxaga, 69
- Lazarian, A. 2007, *JQSRT*, 106, 225
- Lazarian, A., & Hoang, T. 2007, *MNRAS*, 378, 910
- Li, Z.-Y., Krasnopolsky, R., & Shang, H. 2013, *ApJ*, 774, 82
- Loinard, L., Torres, R. M., Mioduszewski, A. J., & Rodríguez, L. F. 2008, *ApJL*, 675, L29
- Mac Low, M.-M., & Klessen, R. S. 2004, *Reviews of Modern Physics*, 76, 125
- Mairs, S., Johnstone, D., Kirk, H., et al. 2015, *MNRAS*, 454, 2557
- Matthews, B. C., McPhee, C. A., Fissel, L. M., & Curran, R. L. 2009, *ApJS*, 182, 143
- Matthews, B. C., & Wilson, C. D. 2000, *ApJ*, 531, 868
- . 2002, *ApJ*, 574, 822
- McKee, C. F., & Ostriker, E. C. 2007, *ARA&A*, 45, 565
- McKee, C. F., Zweibel, E. G., Goodman, A. A., & Heiles, C. 1993, in *Protostars and Planets III*, ed. E. H. Levy & J. I. Lunine, 327
- Miville-Deschênes, M.-A., Martin, P. G., Abergel, A., et al. 2010, *A&A*, 518, L104
- Motte, F., Andre, P., & Neri, R. 1998, *A&A*, 336, 150
- Mouschovias, T. C., & Ciolek, G. E. 1999, in *NATO ASIC Proc. 540: The Origin of Stars and Planetary Systems*, ed. C. J. Lada & N. D. Kylafis, 305
- Naghizadeh-Khouei, J., & Clarke, D. 1993, *A&A*, 274, 968

- Ortiz-León, G. N., Loinard, L., Kounkel, M. A., et al. 2017, *ApJ*, 834, 141
- Ostriker, E. C., Stone, J. M., & Gammie, C. F. 2001, *ApJ*, 546, 980
- Padgett, D. L., Rebull, L. M., Stapelfeldt, K. R., et al. 2008, *ApJ*, 672, 1013
- Pattle, K., Ward-Thompson, D., Kirk, J. M., et al. 2015, *MNRAS*, 450, 1094
- Pattle, K., Ward-Thompson, D., Berry, D., et al. 2017, *ApJ*, 846, 122
- P.Bastien et. al. in prep. 2018, -,
- Planck Collaboration, Ade, P. A. R., Aghanim, N., et al. 2015, *A&A*, 576, A105
- Press, W. H., Rybicki, G. B., & Hewitt, J. N. 1992, *ApJ*, 385, 416
- Rao, R., Crutcher, R. M., Plambeck, R. L., & Wright, M. C. H. 1998, *ApJL*, 502, L75
- Rebull, L. M., Wolff, S. C., & Strom, S. E. 2004, *AJ*, 127, 1029
- Shu, F. H., Adams, F. C., & Lizano, S. 1987, *ARA&A*, 25, 23
- Stamatellos, D., Whitworth, A. P., & Ward-Thompson, D. 2007, *MNRAS*, 379, 1390
- Stutzki, J., & Guesten, R. 1990, *ApJ*, 356, 513
- Tamura, M. 1999, in *Star Formation 1999*, ed. T. Nakamoto, 212–216
- Tamura, M., Hashimoto, J., Kandori, R., et al. 2011, in *Astronomical Society of the Pacific Conference Series*, Vol. 449, *Astronomical Society of the Pacific Conference Series*, ed. P. Bastien, N. Manset, D. P. Clemens, & N. St-Louis, 207
- Tang, Y.-W., Ho, P. T. P., Girart, J. M., et al. 2009a, *ApJ*, 695, 1399
- Tang, Y.-W., Ho, P. T. P., Koch, P. M., et al. 2009b, *ApJ*, 700, 251
- Tang, Y.-W., Ho, P. T. P., Koch, P. M., Guilloteau, S., & Dutrey, A. 2013, *ApJ*, 763, 135
- Vaillancourt, J. E. 2006, *PASP*, 118, 1340
- Vaillancourt, J. E., & Matthews, B. C. 2012, *ApJS*, 201, 13
- Vrba, F. J., Strom, S. E., & Strom, K. M. 1976, *AJ*, 81, 958
- Ward-Thompson, D., Pattle, K., Bastien, P., et al. 2017, *ApJ*, 842, 66
- White, G. J., Drabek-Maunder, E., Rosolowsky, E., et al. 2015, *MNRAS*, 447, 1996
- Wilking, B. A. 1992, *Star Formation in the Ophiuchus Molecular Cloud Complex*, ed. B. Reipurth, 159
- Wolf, S., Launhardt, R., & Henning, T. 2003, *ApJ*, 592, 233